Pharm Res (2014) 31:117–135
DOI 10.1007/s11095-013-1137-x

RESEARCH PAPER

Dissolvable Microneedle Arrays for Intradermal Delivery of Biologics: Fabrication and Application

Bekir Bediz • Emrullah Korkmaz • Rakesh Khilwani • Cara Donahue • Geza Erdos • Louis D. Falo Jr • O. Burak Ozdoganlar

Received: 14 March 2013 / Accepted: 24 June 2013 / Published online: 1 August 2013

ABSTRACT

Purpose Design and evaluate a new micro-machining based approach for fabricating dissolvable microneedle arrays (MNAs) with diverse geometries and from different materials for dry delivery to skin microenvironments. The aims are to describe the new fabrication method, to evaluate geometric and material capability as well as reproducibility of the method, and to demonstrate the effectiveness of fabricated MNAs in delivering bioactive molecules.

Methods Precise master molds were created using micromilling. Micromolding was used to create elastomer production molds from master molds. The dissolvable MNAs were then fabricated using the spin-casting method. Fabricated MNAs with different geometries were evaluated for reproducibility. MNAs from different materials were fabricated to show material capability. MNAs with embedded bioactive components were tested for functionality on human and mice skin.

Results MNAs with different geometries and from carboxymethyl cellulose, polyvinyl pyrrolidone and maltodextrin were created reproducibly using our method. MNAs successfully pierce the skin, precisely deliver their bioactive cargo to skin and induce specific immunity in mice.

Conclusions We demonstrated that the new fabrication approach enables creating dissolvable MNAs with diverse geometries and from different materials reproducibly. We also demonstrated the application of MNAs for precise and specific delivery of biomolecules to skin microenvironments *in vitro* and *in vivo*.

KEY WORDS cutaneous drug delivery · dissolvable microneedle arrays · immunization · micro-fabrication · micromilling

INTRODUCTION

The most prevailing approach for delivering therapeutic biologics and pharmaceuticals into human body follows the parenteral route using hypodermic needles (1,2). However, hypodermic needle-based delivery presents many disadvantages, such as the requirement of trained personnel for administration, the pain and potential tissue damage associated with needle insertions, the possibility of transmission of infectious diseases through needle reuse, accidental needlestick injuries to health-care professionals, and poor patient compliance (1–4). Furthermore, hypodermic delivery is associated with rapid degradation of delivered biologics, which reduces the bioavailability of the delivered drugs/vaccines, necessitating increased doses to obtain the desired effect (1).

B. Bediz · E. Korkmaz · R. Khilwani
Department of Mechanical Engineering, Carnegie Mellon University
Pittsburgh, Pennsylvania 15213, USA

C. Donahue · G. Erdos
Department of Dermatology
University of Pittsburgh School of Medicine Pittsburgh
Pennsylvania 15213, USA

L. D. Falo Jr
Department of Dermatology; Department of Bioengineering
Pittsburgh Clinical and Translational Science Institute
The McGowan Institute for Regenerative Medicine
and the University of Pittsburgh Cancer Institute
University of Pittsburgh School of Medicine
Pittsburgh, Pennsylvania 15213, USA

O. B. Ozdoganlar (✉)
Departments of Mechanical Engineering, Biomedical Engineering, and Materials Science and Engineering, Carnegie Mellon University
Pittsburgh Pennsylvania 15213, USA
e-mail: ozdoganlar@cmu.edu

An attractive alternative to the parenteral route is the cutaneous route (1). There are also substantial clinical advantages to intradermal drug delivery. In addition to eliminating potential issues related to needle-stick injuries and needle reuse, transdermal delivery minimizes or eliminates the need for trained health care professionals for administration of drugs and vaccines. Further, intradermal delivery provides the potential for painless and bloodless delivery that considerably increases patient compliance (1,2).

Although many advantages of transdermal delivery have been recognized, the cutaneous route presents its own challenges: In particular, delivering biologics through the transdermal route requires overcoming the physical barrier created by the *stratum corneum (SC)*—the outer layer of skin—that consists of tightly arranged dead keratinocytes embedded in a complex intercellular matrix that reacts dynamically to the changing environment (5). Without a physical breach (6) or chemical penetration enhancers (7), the SC allows only small molecules (< 500 Da) to penetrate (1,4,8). This places significant limits on the types of therapeutics that can be directly delivered, preventing the use of the cutaneous route for many biologics and particulates without the use of specifically designed delivery-systems and enhancers (9,10).

Pioneering works (8,11–14) presented in the last decade have demonstrated that transdermal delivery using microneedle-arrays (MNAs) can overcome the aforementioned challenges while retaining advantages of cutaneous delivery, thus enabling bolus or sustained delivery of a broad range of biologics through the cutaneous route. These devices include an array of microneedles, with dimensions ranging from 100 to 1,000 μm in width and up to 1 mm in length, that are used to breach the SC, and enable delivery of drugs and vaccines to viable epidermis. There are four major types of MNAs used for transdermal delivery. The first type employs solid or hollow microneedles that pre-condition the skin by piercing the SC and the upper layer of epidermis (15–17). When applied prior to topical application of a biologic-carrier or a conventional patch, the created micro-pores enhance percutaneous drug penetration by increasing the skin's permeability by many orders of magnitude (16,17). However, this passive method provides only limited control of dosage and delivery rate. The second type of MNAs includes solid microneedles that are coated with the biologics to be delivered. This approach provides a better dosage control. In a recent study, immunization using coated MNAs was shown to trigger significantly stronger immune response than that observed in subcutaneous or intramuscular injection (18–20). On the other hand, this approach can only be used to deliver small quantities of drugs. The third type of MNAs utilizes hollow microneedles attached to a reservoir of biologics, thus accommodating better dosage and rate control, as well as considerably higher quantity of delivery cargo (21). Requirements of complex fabrication technology (22), and specialized application settings limit the applicability of reservoir-based microneedle arrays for on-site drug or vaccine delivery (23).

A more advanced MNA alternative is realized by creating microneedles from biocompatible materials that dissolve or biodegrade when inserted into skin. It has been demonstrated that dissolvable MNAs possess sufficient strength to allow insertion, and are dissolved or degraded by the interstitial fluids of the epidermis (1). A range of biocompatible polymers including, singly or in combination, poly-L-lactic acid (PLA) (24–26), poly-glycolic acid (PGA) (24), poly-lactic-co-glycolic acid (PLGA) (24–26), cyclic-olefin copolymer (COC) (27,28), poly (vinyl pyrrolidone) (PVP) (29), poly (vinyl) alcohol (PVA) (30), carboxymethyl cellulose (CMC) (25,31), and silk (32), as well as sugars including galactose (33), maltose (34,35), and dextrin (33) have been used to fabricate dissolvable MNAs. Many different technologies have been used for fabrication of dissolvable MNAs such as photo-lithography (36) and laser etching (38) to create molds and injection molding, investment molding, casting, and hot embossing to create the final needle arrays (27,28,36). The bioactive material to be delivered is encapsulated into the dissolvable (matrix) material through the fabrication process; thus, when dissolved, MNAs deliver the cargo in bolus or sustained fashion. As such, dissolvable MNAs combine the physical toughness of solid microneedles with relatively high bioactive material capacity and controllable delivery rate, while possessing other desired attributes of simple fabrication, storage, and application.

Most recently, there is a growing interest in intradermal delivery strategies to target drugs locally to specific skin microenvironments. In addition to "transdermal" applications of MNA technology that deliver drugs systemically by transdermal routing through skin microvasculature and lymphatic flow, MNAs may be ideally suited for intradermal delivery applications. In particular, MNA delivery strategies capable of overcoming the physical barrier of the stratum corneum that limits topical drug delivery could enable novel approaches for skin targeting vaccines, and more localized treatment of skin diseases. For example, for vaccine applications, the high density of antigen presenting cells (APCs) in skin microenvironments could be targeted directly, thereby multiplying the efficacy of drugs/vaccines/adjuvants and providing a dose-sparing effect, necessitating only a small fraction of the amount of drugs used in hypodermic delivery to obtain the same effect (2–4).

Although many advantages of dissolvable MNAs have been documented through *in-vitro* and *in-vivo* studies, regulatory approval and subsequent clinical applications of MNAs necessitate precise control of deliverable dosage and delivery rate. The delivery rate and amount are dictated by the MNA material, needle geometry, and the array configuration. These requirements translate into the need for high-accuracy, reproducible, and scalable (high-throughput) fabrication techniques applicable to relevant dissolvable materials. An ideal fabrication approach must also enable room-temperature processing without

the use of chemical or biological solvents that can damage bioactivity of the cargo. Furthermore, the fabrication approach should facilitate easy and rapid changes in geometric parameters (for optimization) and should not impose a strict limit on manufacturable designs so that optimal application-driven MNA designs can be achieved.

In this work, we present a novel micromilling/spin-casting based fabrication approach for dissolvable MNAs made from materials that can be processed at room temperature (37). The general approach follows that presented by Prausnitz *et al.* in (38) and Donnelly *et al.* in (30), including fabrication of a set of master molds, which are used to fabricate elastomer production molds. The production molds are then used to cast the aqueous dissolvable material through the spin-casting process, resulting in dissolvable MNAs. A critical departure from the earlier methods is, for the first time, the use of mechanical micromilling technology for the master mold fabrication (38–40). This technology allows creation of complex, high accuracy, three-dimensional geometries on a myriad of materials, including features such as undercuts, fully three-dimensional shapes, high aspect ratios, and sharp tips (38,39). A set of custom fabricated single-crystal diamond micro-endmills are used within a high precision miniature machine tool system to fabricate the master molds. Different needle geometries and array configurations are micromilled and geometrically characterized. Following the fabrication of PDMS production molds, sets of MNAs with different needle and array geometries are fabricated and their reproducibility is quantified. To show material capability, MNAs are fabricated from pure CMC and pure PVP, as well as CMC/PVP and CMC/maltodextrin combinations. We demonstrate the penetration and delivery capacity of these CMC-based MNAs in mouse and human skin, and the immunogenicity of an MNA-delivered biomolecule antigen.

MATERIALS AND METHODS

Fabrication Approach

The fabrication approach used in this work is graphically presented in Fig. 1. The approach involves three distinct processing steps: (1) Creation of master molds from a wear resistant material using the mechanical micromilling process; (2) fabrication of production molds from an elastomer through molding; and (3) fabrication of final dissolvable MNAs from the production molds using the spin-casting technique. The MNA material is prepared by creating a water-based hydrogel using the powder form of the dissolvable material. When included, the bioactive material is mixed with the dissolvable matrix material in its dry powdered form. The hydrogel is loaded into the elastomer molds, and centrifuging in a prescribed temperature is continued until the full density

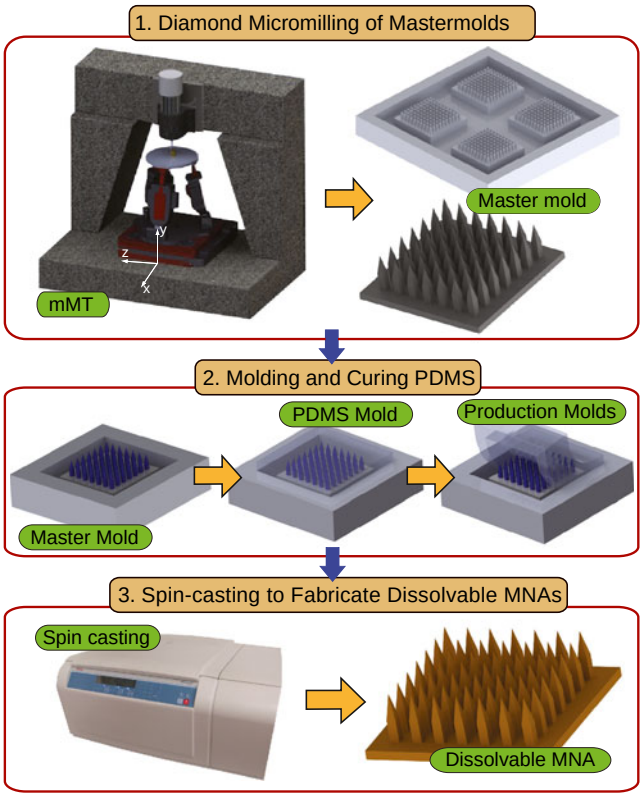

Fig. 1 Description of the presented fabrication approach.

(dry) MNAs are obtained. Since the master and production molds are reusable for a large number of fabrication cycles, the fabrication costs are greatly reduced.

Mechanical Micromilling for Master Mold Fabrication

The master molds were fabricated using the mechanical micromilling process without need for additional or hazardous processing. Micromilling was performed using micro-scale (as small as 10 μm in diameter) milling tools within a high-precision computer controlled custom-made miniature

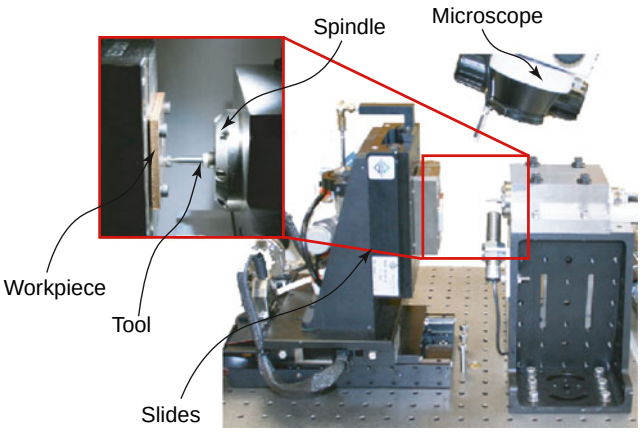

Fig. 2 The custom-built high-precision miniature machine tool system used for fabrication of master molds.

machine tool system with the motion accuracy of 1 µm. As shown in Fig. 2, the system includes three-axis precision slides (Aerotech, ALS-130), a numerical control system (Aerotech, 13846-A-1-1-XYZ), and an ultra-high-speed (UHS) air-bearing spindle (AMS-160, NSK) that is driven by an air-turbine. The tool was attached to the spindle through its meso-scale (3.125 mm diameter) shank via a precision collet. The tool path was designed prior to micromilling, and a G-code based program was written to control the relative motions of the tool and the work piece. The blank work piece was attached to the three-axis slides using clamps. After completion of contact-finding and tool indication procedures, the process continues in a completely automated fashion.

The master mold geometry, shown in Fig. 1, includes four arrays of microneedles, as well as channels that surround the arrays. In the production molds, the channels become raised pockets that act as a reservoir for the hydrogel. Poly(methyl methacrylate) (PMMA, 8560K274, McMaster Carr) was used as the master mold material. A tungsten-carbide micro-tool with 1 mm diameter (TR-2-0400-S, PMT) was used to level the surface by milling out a small amount of material from the work piece, and subsequently, to create the channels. When fabricating the channels, full-immersion milling with feed rate of 24 µm-per-revolution (feed speed of 32 mm/s), spindle speed of 80,000 rpm, and an axial depth of cut (per pass) of 50 µm was used. The master molds for the MNAs were then created on the four protrusions left on the work piece surface.

To obtain accurate and defect-free microneedles on the master mold, a set of tailor-made single-crystal diamond micro-endmills (straight and tapered diamond micro-endmills) were designed and fabricated (see Fig. 3). For microneedles with pyramidal geometry, only tapered diamond micro-tools with 15 deg. and 22.5 deg. taper (apex/pyramid) angles were used. Both the 15 deg. and 22.5 deg. tools had a 300 µm cutting diameter at their base. For both tools, cutting depths up to 1.5 mm could be attained. For the straight obelisk and the (negative) beveled obelisk microneedle geometries, in addition to the tapered diamond micro-tools (that create the tip/apex portion of the microneedles), a straight (for the straight obelisk, with a cutting diameter of 450 µm) or a negative tapered (for the negative beveled obelisk, with a base cutting diameter of 850 µm and a taper angle of –5 deg.) diamond micro-tool was used to obtain the stem portion of the microneedles. Each diamond tool has only one cutting edge. A specific feature designed in these tools is a rounded corner, which creates a fillet at the base of each needle on the master molds, and thus, on the final dissolvable MNAs. This fillet considerably increases the effective strength of the needles during insertion.

After the completion of the micromilling process, the master molds were cleaned using an ultrasonic cleaner (SRA - Trupower UC-20D Ultrasonic Cleaner). In order to remove any residual chips that may still exist on the master molds, a subsequent cleaning step was completed by following the elastomer molding procedure described below. This sacrificial mold was then discarded.

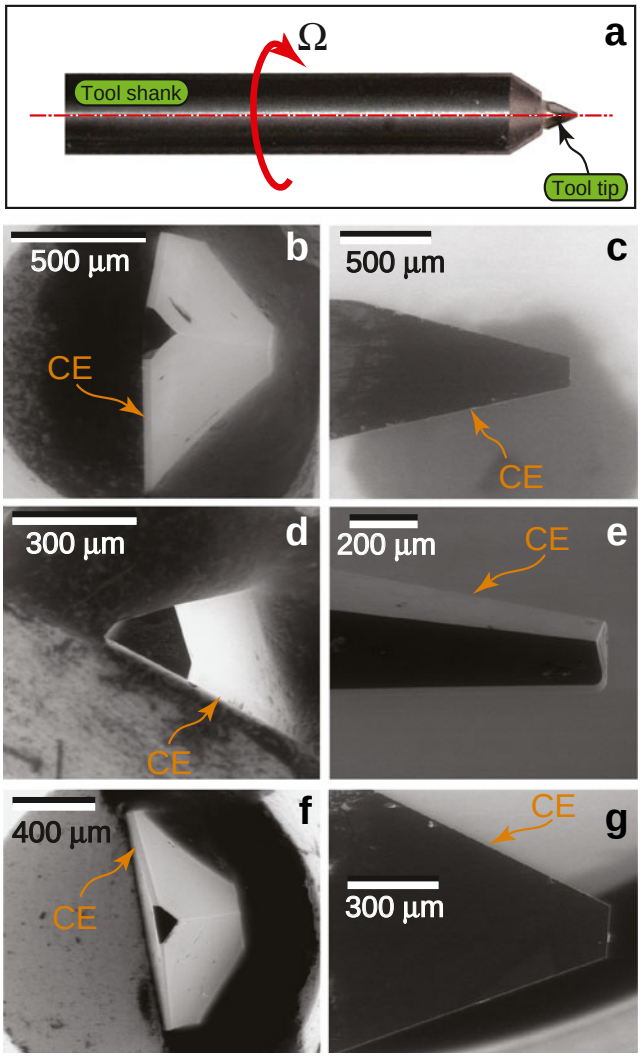

Fig. 3 Geometries of custom-made diamond tools (*CE* indicates the cutting edge). (**a**) Overall view of a diamond micro-tool with meso-scale tool shank, (**b**–**c**) top and side views of a V-shaped tool with 15° apex angle and 300 μm diameter, (**d**–**e**) top and side views of a straight diamond tool with 450 μm diameter, (**f**–**g**) top and side views of a straight diamond tool with 5° back rake angle and 850 μm diameter.

Fabrication of Production Molds

The production molds were fabricated from polydimethylsiloxane (PDMS), which was obtained using SYLGARD® 184 (Dow Corning), a two component clear curable silicone elastomer. The base material was mixed with a curing agent in 10:1 SYLGARD®-to-curing agent ratio. Subsequently, the mixture was degassed for 10 min and poured over the master mold to form an approximately 8 mm layer. This was followed by another step of degassing for 10 min. Next, the master mold with the degassed mixture was placed in an oven, and cured at 75°C for 1 h. After cooling down to room temperature, the

cured PDMS was separated from the master mold. Due to the specific geometry of the master molds, each replication produced four arrays of MNAs simultaneously.

Preparation of Dissolvable Materials for MNAs

In this work, two dissolvable polymers and a natural polysaccharide were used to demonstrate the fabrication approach and geometric diversity, as well as to quantify the fabrication accuracy and reproducibility. MNAs were fabricated from carboxymethyl cellulose (CMC, cat# C5678, Sigma-Aldrich, St Louis, MO), polyvinylpyrrolidone (PVP, cat# 856568, Sigma-Aldrich, St Louis, MO), three CMC/PVP combinations, and a CMC/maltodextrin (cat# 419699, Sigma-Aldrich, St Louis, MO) combination. In each case, the preparation began by using the dry powdered form of the material. The powders were thoroughly mixed manually using a spatula. Based on the specific weight ratio selected for the hydrogel, an amount of deionized (DI) water was added to the powder to achieve the desired concentration and then thoroughly mixed using a spatula. The obtained hydrogel was refrigerated at 4°C for 24 h for the mixture to equilibrate, and subsequently centrifuged at 2000*g* for 30 min to remove the occasional bubbles from the hydrogel. For the CMC hydrogel, a 33 wt% mass concentration was used, whereas PVP was prepared at 25 wt% mass concentration. The hydrogels for CMC/PVP combinations was prepared by mixing 75/25, 60/40, or 50/50 wt%/wt% ratios of CMC and PVP into DI water at 25 wt% final solute concentration. The CMC/maltodextrin hydrogel was prepared using a 50 wt% CMC and 50 wt% maltodextrin mixtures in DI water at 25 wt% solid concentration.

To demonstrate the bioactive cargo encapsulation and delivery, ovalbumin (cat# A5503, Sigma-Aldrich, St Louis, MO) was used as the model cargo; this application includes only CMC as the matrix material. The hydrogel was prepared by mixing powdered forms of 10 wt% ovalbumin and 90 wt% CMC. This powder was then added to sterile distilled water at 25 wt% solute concentration. The prepared hydrogel was refrigerated at 4°C for 24 h for the mixture to equilibrate and for bubbles to be removed.

Spin Casting

The final molding of dissolvable MNAs was performed through the spin-casting process using a centrifuge (ThermoFisher Scientific – Heraeus Multifuge X3R with Swinging Bucket Rotor TX 750). The prepared hydrogel was loaded into the PDMS production molds. Considering the geometry of the molds, sufficient amount of hydrogel was dispensed over the production mold. Accordingly, for each MNA, 80 μl of hydrogel was placed over the mold. To ensure that the centrifugal force acts along the axis of the needles, a set of PDMS inserts were fabricated and placed inside the centrifuge buckets. For this purpose, sufficient amount of liquid elastomer was filled in the buckets, and was cured at the room temperature while the centrifuge rotates as the selected operating speed (4,700 rpm). Thus obtained inserts have flat surfaces that are perpendicular to the centrifugal force when rotating at the operating speed. The production mold was then placed on top of the inserts inside the centrifuge buckets, and centrifuged for 8 h at 5°C or at the desired temperature, which was sufficient to obtain MNAs with above 98% dryness ratio.

Imaging and Dimensional Measurements

Qualitative and quantitative assessment of the MNA geometries and reproducibility was performed by obtaining scanning electron microscope (SEM) images of MNAs and individual needles, and by using an image processing algorithm. The environmental SEM (Quanta 600) with its field-emission capability enabled obtaining MNA images without a conductive coating. High resolution images of complete arrays, individual needles, and needle tips were used in qualitative assessment of MNA geometries. Using image processing tool box in MATLAB® and high-resolution SEM images, measurements of tip radius, tip (wedge) angle, and width of individual needles were performed. A sample set of measurements are shown in Fig. 4.

Microneedle arrays with three different types of needle geometries (pyramid, straight obelisk, and negative-beveled obelisk), with different geometric parameters (width, height, and apex angle; see Fig. 5) and with different array configurations were fabricated for qualitative and quantitative assessment (see Table I). Two levels of reproducibility analysis were conducted: The first level involved evaluation of geometric accuracy of master molds fabricated by micromilling. For a given set of geometric parameters, the apex angle and width of at least one-third of the microneedles in an array were measured and measurements were compared to the target dimensions. A statistical analysis of results was subsequently completed to determine the statistical distribution of results (average width and apex angle, as well as their standard deviations). To further assess reproducibility across different arrays within a mold and across different molds, further measurements from another array on the same molds, and two arrays on different molds, were conducted and the results were evaluated following statistical characterization above. Furthermore, tip radii of microneedles were measured.

The second level analysis of reproducibility involved geometric analysis of CMC MNAs. In this case, 20 microneedles from three different fabricated arrays were measured (width and apex angles) and reproducibility and shrinkage (with respect to the master mold dimensions) were analyzed statistically. Tip radii of nine needles were also measured from three different arrays.

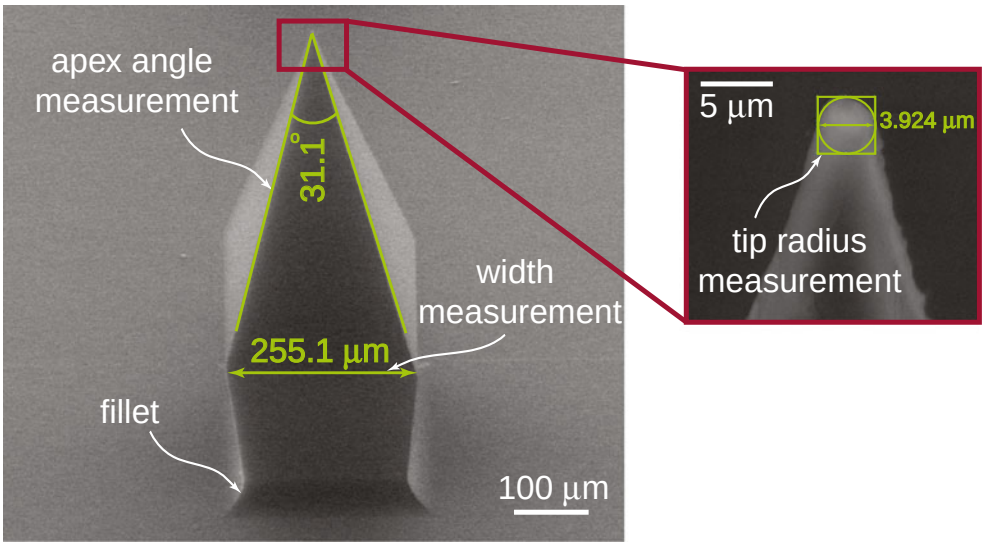

Fig. 4 Sample SEM measurements of width, apex angle, and tip radius of MNAs. An image-processing code is used to identify and quantify the measured shapes and features.

Mice and Animal Husbandry

Female C57BL/6 mice, age 6–8 weeks, were purchased from The Jackson Laboratory (Bar Harbor, ME) and housed in the pathogen-free animal facility of the University of Pittsburgh and used according to the institutional guidelines with approval of the University of Pittsburgh Institutional Animal Care and Use Committee.

Image Analysis of MNA Delivery to Mouse and Human Skin

We initially evaluated MNA cargo delivery by examining delivery of MNA embedded dye to human skin. To accomplish this, MNAs with embedded 1 vol% India ink as tracer dye were prepared from 20 wt% CMC-hydrogel using the spin-casting fabrication method described above. Preparation of human skin explants was described elsewhere (41). Briefly, living human skin was obtained as freshly excised plastic surgery residuals under IRB approval and used according to the Univ. of Pittsburgh Medical Center guidelines. Human skin explants approximately 2 mm thick and 20 mm×20 mm surface area were prepared using a dermatome. The resulting living human skin samples were comprised of unaltered epidermis and underlying dermis, maintained in a normal physiologic state by culture at an air-fluid interface. For MNA delivery, MNAs with embedded tracer dye were applied using a spring-loaded applicator. The travel distance of the impact head of the applicator was limited to 1.5 mm. After 15 min, MNAs were removed and were sputter-coated with gold and imaged by SEM (JEOL 9335 Field Emission SEM) at the Center for Biologic Imaging, University of Pittsburgh. Targeted skin explants were processed for macrophotographic imaging using a CCD camera-equipped Zeiss preparative stereo microscope at 5× optical magnification.

For anatomic evaluation, MNAs with obelisk needle geometry were prepared with integrated green fluorescent particles (Fluoresbrite YG 1 µm, Polysciences Inc., cat#. 15702) at 0.5×10^6 particles/ml in 20 wt% CMC hydrogel, and particle embedded MNAs were fabricated using the spin casting method described above. To evaluate MNA delivery to mouse skin, groups of mice were anesthetized, and MNAs were applied to

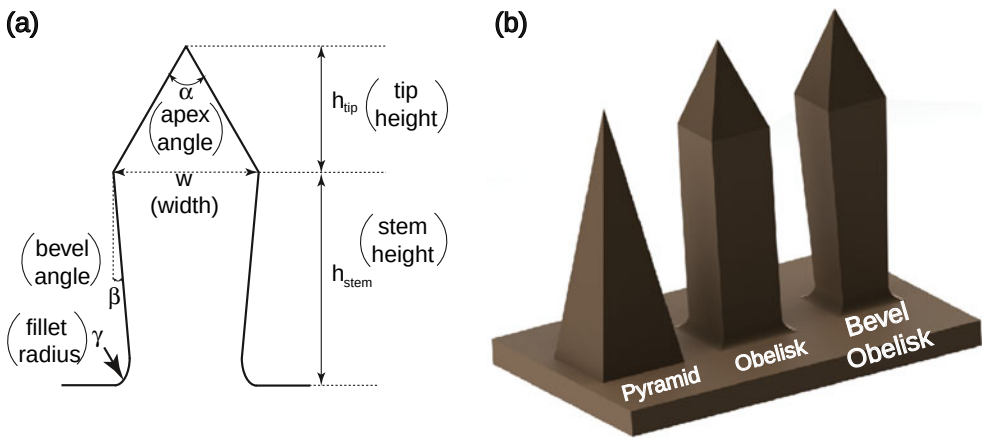

Fig. 5 (**a**) Parameterized geometry of a microneedle, and (**b**) the three types of shapes considered in this study.

Table I Target Geometries and Parameters for the MNA Master Molds

Design	Microneedle geometry	Apex angle (degrees)	Width (μm)	Total height (μm)
1	Pyramid	45	500	600
2		30	315	600
3	Straight obelisk	30	170	600
4		30	210	700
5		30	150	850
6	Beveled obelisk	30	250	750
7		45	260	760

mouse ears using a spring-loaded applicator. After 10 min, MNAs were removed, mice were sacrificed, and excised target skin was processed for microscopy. In some cases, skin was imaged directly using an inverted microscope fitted with a charge-coupled device (CCD) camera. In others, skin samples were further processed and cryosectioned to prepare the samples for fluorescent microscopy.

To evaluate MNA delivery to living human skin, fluorescent particle containing MNAs were applied to skin as described above. Targeted skin was excised using a 10 mm biopsy punch and processed for cryo-sectioning. Sections were stained with 0.1% toluidine blue for light microscopy and imaged with a Nikon transmission fluorescent microscope. In some cases, DAPI stained sections (300 nM DAPI (Invitrogen, cat.# D1306)) were further processed and stained with PE labeled anti-HLA-DR for human skin (BD Pharmigen) or PE labeled anti-Ia for mouse skin (BD Pharmigen) to visualize antigen presenting cells.

Quantitative Measurement of MNA Delivery to Human Skin

To quantitatively evaluate the effects of pyramidal and obelisk needle geometry on MNA delivery, CMC hydrogel was prepared with 5 wt% ovalbumin (OVA) with ^{3}H-tracer to yield 25 wt% final dry-weight content (5 g/95 g OVA/CMC) with 0.5×10^{6} dpm/mg. From a single stock four batches of MNAs were fabricated, containing several individual MNAs of pyramid and obelisk needle geometries. The MNAs were applied to human skin as described above. The target area was tape-stripped to remove surface debris and then excised using a 10 mm biopsy punch, and the ^{3}H content was determined by scintillation counting.

Kinetics of MNA Delivery

MNAs were fabricated with OVA and trace-labeled Alexa488-OVA (Invitrogen, cat# 034781) (OVA 50 μg/MNA) and varying structural components (CMC only, 50% CMC + 50% maltodextrin, 75% CMC + 25% PVP and 50% CMC + 50% PVP) as described above. Alexa488-OVA labeled MNAs were applied to human skin samples in quadruplicate for each treatment for 5, 10, 20 or 40 min and then removed. The targeted skin area was sampled using a 6 mm biopsy punch and Alexa488 dye was released from the samples by ProteaseK digest at 37°C overnight. The protease treated samples were cleared from the high molecular weight nucleic acid residues by the addition of equal volume of iso-propanol and centrifugation at 12,000*g* for 10 min. The cleared samples were dispensed into 96 well plates and quantitated by measuring the fluorescent signal emission at 535 nm. The excitation wavelength of Alexa488 was 487 nm. The OVA transfer efficiency to the skin explants was expressed as % of OVA content of the MNAs. The datasets were statistically analyzed using two-way ANOVA tests.

Integrity of MNA Embedded OVA

The integrity of OVA during the MNA fabrication process was determined by SDS PAGE and OVA-specific ELISA assays. Briefly, for SDS PAGE, freshly prepared OVA stock solution (100 mg/ml), OVA CMC-hydrogel (50 mg/ml) and OVA-MNA (50 μg/MNA) rehydrated in PBS were diluted in PBS to 10 mg/ml. Under reducing conditions, 5 μg OVA per sample was loaded into the wells of a pre-cast 12% polyacrylamide gel (BioRad, cat #456-1043) and run in a BioRad Mini-PROTEAN electrophoresis tank. The proteins were visualized by staining with Coomassie Brilliant Blue R250 (BioRad, cat # 161-0436). OVA-specific ELISA was accomplished using biotin labeled anti-OVA antibody (Pierce, cat. # PA1-26972) at 10,000× dilution as recommended by the manufacturer. OVA binding was determined after serial dilutions in Na-bicarbonate/carbonate coating buffer (100 mM, ph9.6) at the nominal concentration range between 300 and 0.137 ng/ml on ELISA plates. After binding the samples, plates were blocked with 1% BSA in PBS. Avidin-Horseradish Peroxidase (BD Pharmingen, cat # 554058) was used as reporter according to the manufacturer's recommendation. P-values determined by two-way ANOVA.

MNA-Directed Skin Immunization

OVA-embedded MNAs incorporating 50 μg of ovalbumin were prepared as described above. OVA specific cellular immunity was determined in groups of four 6–8 week old female C57Bl/6 mice, either immunized by OVA-MNA application to the skin, or by intramuscular injection of OVA into the hind limbs gastrocnemius muscle of the same quantity of OVA in PBS, or left untreated. Mice were boosted on day 7 and then assayed for *in vivo* OVA-specific T-cell lytic activity 5 days later using well established techniques (41–45). Briefly, splenocytes from naïve mice were

pulsed with 2 μg/ml OVA derived SIINFEKL peptide epitope, or left unpulsed for 1 h. The antigen pulsed splenocytes were washed and stained with high concentration CFSE (10 μM), while the unpulsed slenocytes were labeled with low concentration CFSE (1 μM) for 15 min at 37°. Equal populations of the pulsed and unpulsed target cells were injected intravenously into immunized and naïve mice at a final concentration of 2×10^7 splenocytes/per mouse. Twenty hours after the injection, the spleens were recovered from all the animals, and the killing of target cells was evaluated by comparison of the antigen pulsed and unpulsed populations by flow cytometry to quantify antigen specific killing of the high CFSE labeled SIINFEKL-pulsed targets. Specific lysis was calculated according to the following formula: $\{1-[(\text{ratio of } CFSE^{low}/CFSE^{high} \text{of naïve mouse})/(\text{ratio of } CFSE^{low}/CFSE^{high} \text{of vaccinated mouse})]\}\times100$ and expressed as % of maximum lysis. Data is representative of 3 experiments and was statistically analyzed using two-way ANOVA ($P<0.05$).

RESULTS

Fabrication and Characterization of Master Molds

Micromilling of Master Molds

We utilized the mechanical micromilling process for the master mold fabrication. This is a critical departure from the previous applications of spin-casting-based fabrication of MNAs. Similar to the conventional milling process, a rotating cutting tool is moved along a prescribed path to remove material from the work piece, leaving behind the desired geometry. In micromilling, however, the cutting tool is at micron scale, and the spindle speeds are ultra-high (e.g., 150,000 rpm).

We selected PMMA as the master mold material due to its good machinability, strength, and wear-resisting characteristics. A 9 mm thick PMMA workpiece with 25 mm × 25 mm dimensions was placed on the platform of the custom-made miniature machine tool. To increase the production rate, the design of the master mold included four microneedle arrays, thereby allowing simultaneous creation of four dissolvable MNAs from a single production mold. A carbide endmill with 1 mm diameter was attached to the UHS spindle, and the tool-workpiece contact was established. After a leveling cut to create a smooth and flat face on the work piece surface, 1.5 mm-deep channels with the pattern shown in Fig. 1 were milled: in the production molds, these trenches become raised walls, which create a reservoir for the loaded hydrogel. Since the accuracy of microneedles on the master mold is critical, in lieu of the tungsten-carbide micro tools, a set of custom made single-crystal diamond tools were used to fabricate the microneedles on the master mold (see Fig. 3).

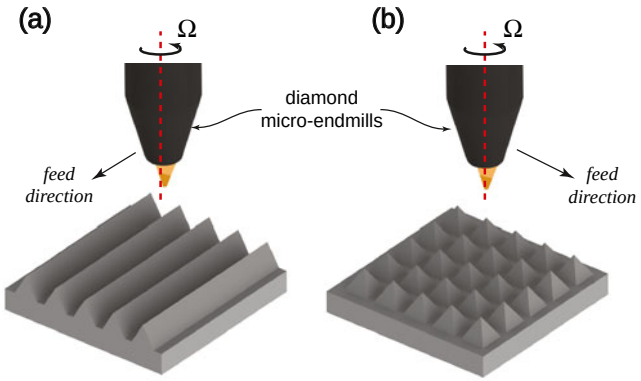

Fig. 6 The tool paths used during micromilling of master molds.

The tool paths utilized to obtain different needle geometries and array configurations are depicted in Fig. 6. For microneedles with pyramidal geometry, only one, tapered diamond micro-tool is used. The apex (included) angle of the pyramids becomes equal to twice the taper angle of the micro-tool. The tool was first moved along the *x*-direction with a spindle speed of 100,000 rpm, axial depth of cut of 20 μm, and feed rate of 9 μm per-revolution (equivalent to a feed speed of 15 mm/s). Each tool pass generates a V-shaped channel by the rotation of the tapered tool. After the completion of each channel, the tool was advanced by a specified amount in the *y*-direction (as dictated by the array configuration) to make a set of parallel V-channels. Once the channels in the *x*-direction were completed, similar channels in the *y*-direction were fabricated. This process was continued, removing material in each pass, until the required amount of material was removed to obtain the desired microneedle height. This process generates square-base pyramidal microneedles. If desired, the tool path can be modified to create microneedles with any convex pyramid with uniform or non-uniform sides.

Two other types of microneedle geometries are demonstrated in this paper, including a straight obelisk and a (negative) beveled obelisk (see Fig. 5). For either of these geometries, the initial part of the process follows that for the pyramid geometries to create the tip portion of the microneedles. Subsequently, a straight (for the straight obelisk) or a negative-tapered (for the negative-beveled obelisk) diamond micro-tool is used to fabricate the stem portion of the obelisk microneedles. When creating the stem portion, a tool path similar to that for the pyramidal portions is followed using an axial depth of cut (per pass) of 20 μm, a spindle speed of 100,000 rpm, and a feed rate of 12 μm-per-revolution (feed speed of 20 mm/s). The total number of passes is selected to obtain the required stem height.

Analysis of Needle Strength

The mechanical strength of the final microneedles is critical to the successful application of MNAs through skin. The

final MNAs should demonstrate sufficient strength for penetrating the stratum cornea without mechanical failure. In our preliminary tests, the dominant failure mode for the obelisk microneedles was caused by bending. Bending stresses induce failure at regions with high stress concentration. Indeed, the highest stress concentration, and thus the failure, occurred at the location where the microneedles meet the substrate through the sharp intersection. To ensure the application of needles without failure, we conducted a finite-elements analysis (see Fig. 7). In this mechanical analysis, the stress distribution of dissolving MNAs, as well as the effect of adding a fillet to the microneedles on stress distribution is determined (using the mechanical properties of CMC given in (31)). To consider a realistic force distribution during insertion, the forces were provided in a non-symmetric fashion to the microneedle tip region. In these computer simulations, inclusion of the fillet increased the apparent strength of the microneedles significantly. As depicted in Fig. 7, the factor of safety for needles with fillets is two times higher than that of needles without fillets (the maximum stress values are 17.28 MPa and 33.70 MPa for the microneedles with and without a fillet, respectively). Accordingly, the diamond tools are designed to include a rounded corner: This rounded corner generates a fillet at the bottom of the needles, where the needles meet the substrate. Based on this analysis, a fillet radius of 35 μm is chosen and fabricated on the master molds, and thus on the final MNAs (see Fig. 7).

Geometric Characterization of Master Molds

Figure 8 shows the SEM images of the fabricated master molds. An important prerequisite to create clinically relevant dissolvable MNAs is to fabricate accurate and reproducible master molds with required microneedle array geometries. To assess the accuracy and repeatability of the master molds, we measured and statistically characterized geometric parameters of the microneedles (1) within the same array, (2) between different arrays in the same mold, and (3) between different molds. The MNA images were taken using an environmental SEM without applying a conductive coating to the needles. The width and apex (tip) angle of each needle, the latter of which is an indication of the needle sharpness, were measured. In each case, 36 needles were measured from an array. This data was used to determine the statistical distribution of parameters. To assess the effect of needle shape on accuracy and repeatability, the geometric evaluation was completed separately on each of the three types of needle designs. Furthermore, geometric parameters were varied to obtain a total of seven different needle geometries given in Table I.

Figure 9 shows a sample statistical distribution for the needle width and apex angle. In each case, a normal-distribution curve was fitted to determine the average and standard deviation of the parameters of interest. The Jarque-Bera test (a goodness of fit test to test normality of a sample) was conducted to determine whether the distribution of each parameter can be considered as a normal distribution: It was seen that the apex angle and width measurements show a normal distribution with 95% significance level.

The targeted dimensions and the measured data for different microneedle geometries are summarized in Table II. For the apex angle, the maximum departure from the target was seen to be 2.73 deg. in average. However, it was seen that the maximum standard deviation was less than 0.79 deg. in any of the cases. The small difference between the targeted and actual apex angles can be attributed to two sources: (1) the deviation of the taper angle of the micro-tool due to tool-fabrication inaccuracies, and (2) the deflection of the needles during micromilling. The maximum difference between the targeted and the average widths was seen to be 1.00% of the average needle width. In any of the cases, the standard deviation was below 3.46 μm of the target width, with an average standard deviation of 2.04 μm.

To evaluate the reproducibility of master molds across different arrays within the same mold and across different molds,

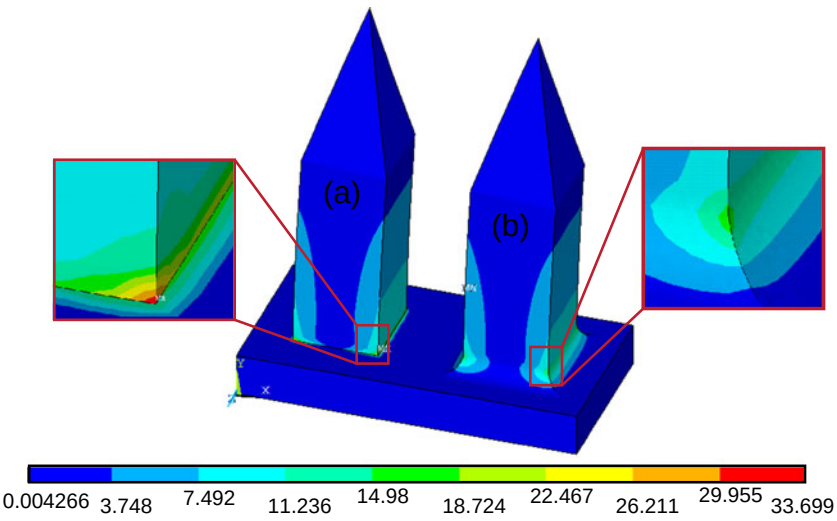

Fig. 7 The stress distribution obtained from the finite element analysis of microneedles: (**a**) without a fillet and (**b**) with a fillet. The colors indicate von Misses stress levels in MPa. The filleted edge provides significant reduction in overall stress, and thus, increases the apparent strength.

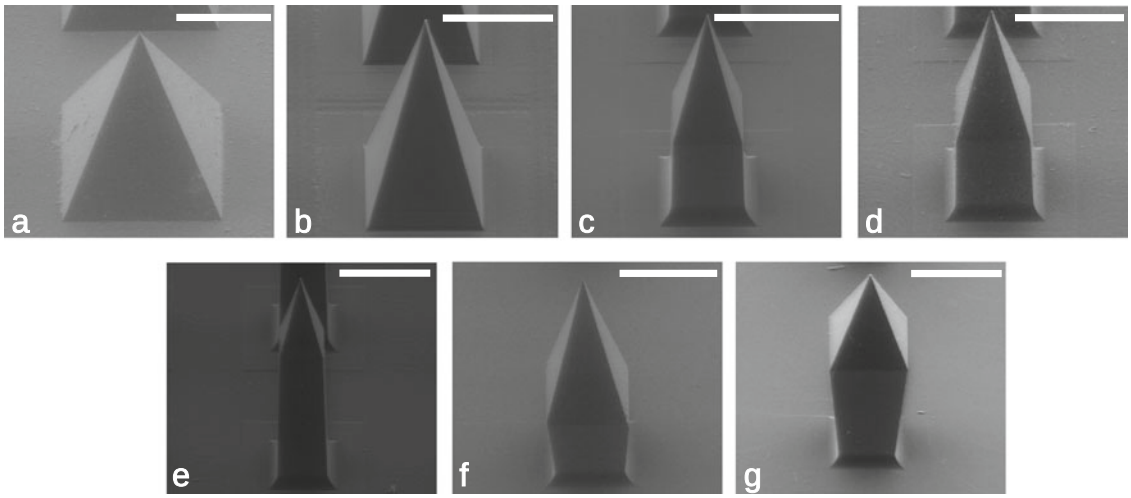

Fig. 8 SEM images of master molds for MNA geometries specified in Table I: (**a**) a pyramid needle with 45° apex angle, (**b**) a pyramid needle with 30° apex angle, (**c**) a straight obelisk needle with 30° apex angle, 200 μm width, and 600 μm height, (**d**) a straight obelisk needle with 30° apex angle, 250 μm width, and 700 μm height, (**e**) a straight obelisk needle with 30° apex angle, 250 μm width, and 850 μm height, (**f**) a beveled obelisk needle with 30° apex angle, 250 μm width (base width is 200 μm), and 752 μm height, (**g**) a beveled obelisk needle with 45° apex angle, 250 μm width (base width is 170 μm), and 760 μm height (each scale bar corresponds to 300 μm).

five needles from another array (out of four) on the same mold, and five needles on each of the two arrays on a separate mold were measured and compared to the original distribution. In each case, it was seen that the data falls within the 95% confidence band ($\pm 2\sigma$) of the data measured from the first array. This is illustrated in Fig. 10, where the data for each geometry is scaled about its own average (the (0,0) point in the graph) and presented as a variation about its average. Here, the square indicates the 95% confidence interval in width and apex angle. It is seen that, out of 105 data points (7 geometries, 5 measurements in each of 3 arrays) only 4 points lie outside of $\pm 2\sigma$ range. Based on these results, it can be concluded that the master molds can be made with very high accuracy and repeatability. In addition, the reproducibility within the same mold and across different molds has been established.

The tip sharpness of the MNAs is also critical in determining the penetration force and depth of penetration. The tip shapes and geometry created through micromilling are not dictated directly by the cutting geometry, but by the inherent characteristics of cutting mechanics; therefore, it is important to characterize the tip radii on the master molds. The challenge in measuring tip radius using SEM is that, at higher magnifications needed to determine the tip radius, the accelerated electrons damage the tip by removing material, thus rendering it blunter. As a result, the master mold becomes unusable. For this reason, only a small number of tips were measured to obtain an estimate of tip radii of the needles on the master mold. Randomly chosen five needles from an array with the geometry of case 5 (30 deg. apex angle, straight obelisk) and five needles from an array with the geometry of case 7 (45 deg. apex angle, negative-beveled obelisk) were measured. It was seen that the average tip radii were 4.5 µm and 5.5 µm for the 30 deg. and 45 deg. needles, respectively. The maximum deviation from the average was 1.2 µm, which was observed for the 45 deg. needles. This indicates that micromilling is capable of creating sharp tips on master molds.

Geometric Characterization of Dissolvable MNAs

A direct characterization of the final geometries of dissolvable MNAs fabricated through micromilling/spin-casting route was performed. For this purpose, CMC MNAs from each of the seven geometries were fabricated using the

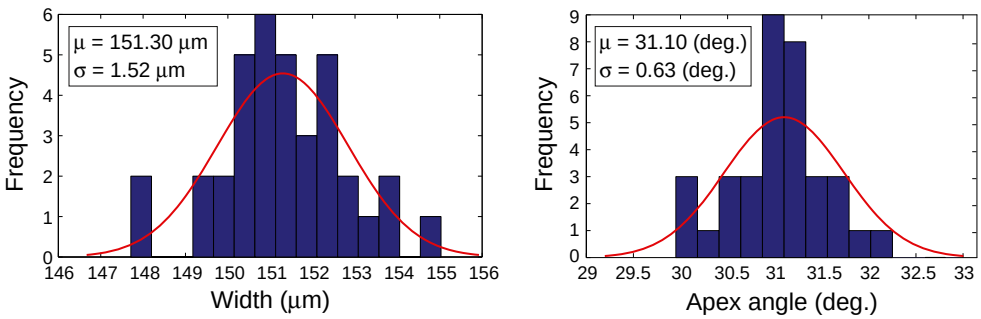

Fig. 9 Sample statistical distributions of widths and apex angles (for the straight obelisk with 30° apex angle, 150 μm width, and 850 μm height).

Table II Mean Values and Standard Deviations of Apex Angles and Widths of Needles in Master Molds

Design	α_{target} (deg.)	μ_α (deg.)	σ_α (deg.)	% Diff. in α	w_{target} (μm)	μ_w (μm)	σ_w (μm)	% Diff. in w
1	45	45.52	0.35	1.16	500	502.23	3.46	0.45
2	30	31.33	0.15	4.43	315	313.58	1.21	−0.45
3	30	30.41	0.68	1.37	170	169.58	1.74	−0.25
4	30	32.16	0.73	7.20	210	210.88	2.37	0.42
5	30	31.10	0.63	3.67	150	151.30	1.52	0.87
6	30	32.73	0.33	9.10	250	252.49	1.69	1.00
7	45	45.74	0.79	1.64	260	262.32	2.27	0.89

described fabrication process. A set of PDMS production molds were fabricated from each of the master molds characterized above. CMC hydrogel was then prepared, and loaded onto the production molds. After completion of the spin casting, the solid (dry) CMC MNAs were separated from the production molds. For each microneedle geometry, a single master mold was used, and all four of the MNAs obtained from the mold were considered during the characterization study. Fabricated microneedles are shown in Fig. 11. To incorporate the variations between different arrays in a set of MNAs from the same master mold, we measured a total of 20 needles from the four MNAs. Both width and apex angle of the needles were quantified. Table III summarizes the measured data.

In each case, the apex angles on the dissolvable microneedles were seen to be smaller than those on the master molds used to fabricate the MNAs. This is an expected result due to the shrinkage of the CMC while drying. It is seen that the reduction in apex angles were considerably larger for the needles that has 30 deg. target apex angle. This reduction effectively renders the needles sharper than those on the master mold geometries. Importantly, the standard deviation on the apex angles was below 1.65 deg. for all of the studied cases, with an average standard deviation of 0.93°.

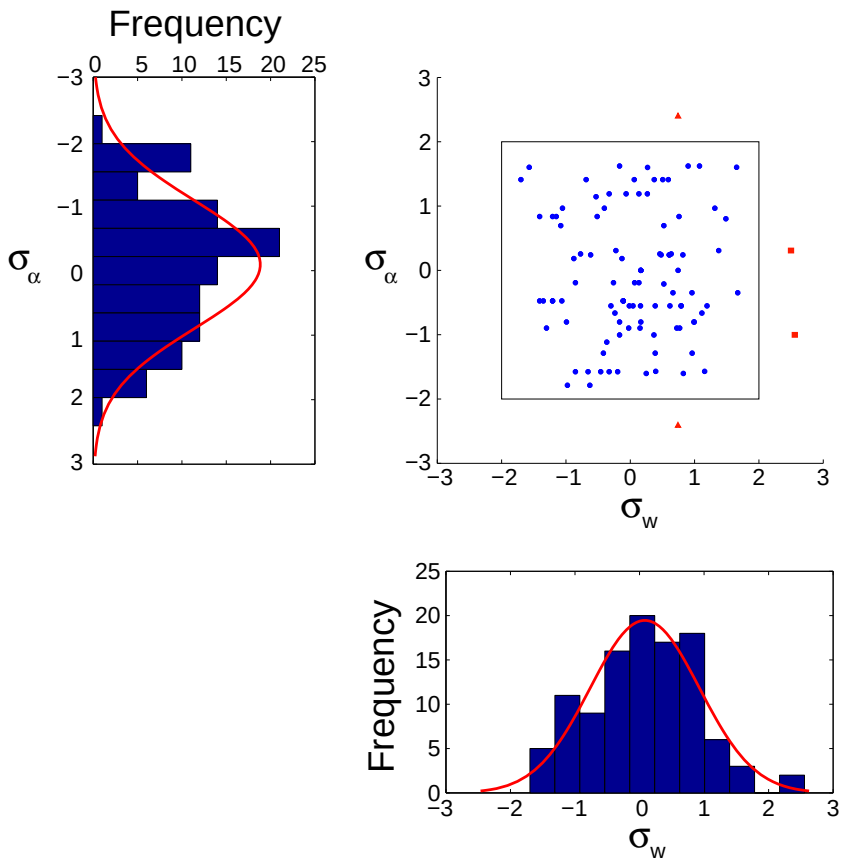

Fig. 10 Distribution of measured data with 95% confidence interval for the measured microneedles. Only four out of 105 needles (measured separately and not included in calculation of the confidence bands) were seen to be outside of the 95% confidence bands.

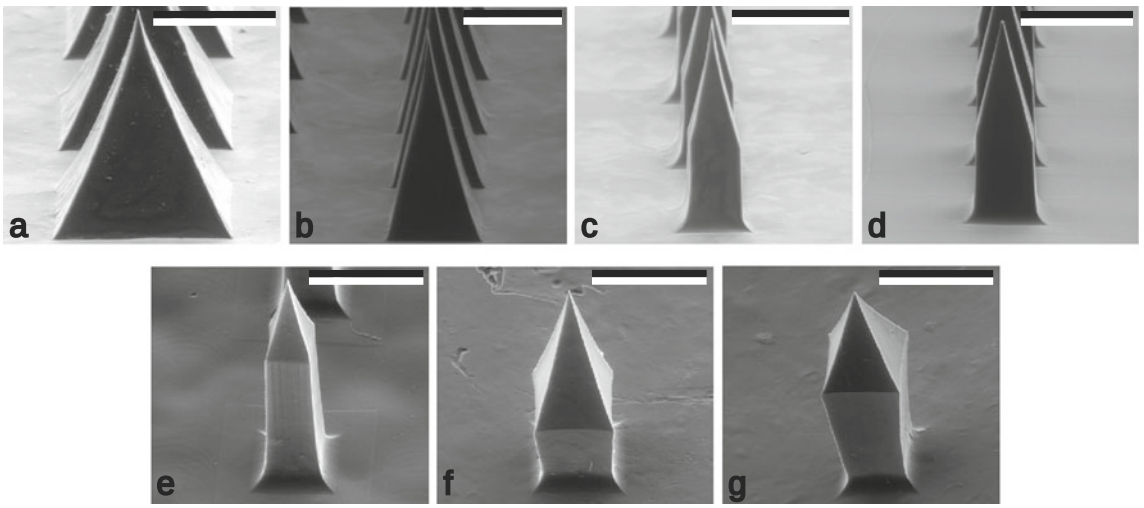

Fig. 11 SEM images of dissolvable microneedles from CMC MNAs based on the parameters in Table I: (**a**) a pyramid needles with 45° apex angle, (**b**) a pyramid needle with 30° apex angle, (**c**) a straight obelisk needle with 30° apex angle, 200 μm width, and 600 μm height, (**d**) a straight obelisk needle with 30° apex angle, 250 μm width, and 700 μm height, (**e**) a straight obelisk needle with 30° apex angle, 250 μm width, and 850 μm height, (**f**) a beveled obelisk needle with −5° bevel angle, 30° apex angle, 250 μm width (base width is 200 μm), and 752 μm height, (**g**) a beveled obelisk needle with −5° bevel angle, 45° apex angle, 250 μm width (base width is 170 μm), and 760 μm height (scale bars correspond to 300 μm).

As much as 23% shrinkage was observed in the needle widths. It was seen that the obelisk and beveled obelisk needles exhibit larger shrinkage (average of 19.59% in base width) than the pyramidal needles do (average of 11.01% in base width). However, it is critical to note that the maximum standard deviation of the needle widths was 5.10% of the average width (for case 1), with an average standard deviation of 3%. The largest standard deviation was observed for case 6 on the dissolvable MNAs.

The tip radii of fabricated MNAs were also measured. For this purpose, nine needles were measured from each of the 30 deg. and 45 deg. microneedle geometries (considering cases 5 and 7). It is seen that the average tip radii were 3.1 μm and 3.2 μm for the 30 deg. and 45 deg. MNAs, respectively. The maximum deviation from the average was 1.1 μm, which was observed for one of the 45 deg. needles. Clearly, the shrinkage induced further sharpness to the needles by also reducing the tip radii from the master mold to final MNAs.

Dissolvable Microneedle Arrays from Different Materials

The selection of MNA materials is dictated by functional requirements, including type of bioactive cargo to be encapsulated, dissolution (release) time, dissolution by-products, and mechanical characteristics of the material. In this section, we demonstrate the application of the presented micromilling/spin-casing fabrication approach for creating dissolvable MNAs from different materials. For this purpose, we created MNAs from (1) CMC; (2) PVP; (3) CMC/PVP at 75/25 dry-weight ratio; (4) CMC/PVP at 60/40 dry-weight ratio; (5) CMC/PVP at 50/50 dry-weight ratio; and (6) CMC/maltodextrin at 50/50 dry-weight ratio. For each material, MNAs from all of the seven geometries were fabricated. Figure 12 shows sample images for three types of geometries (cases 2, 4 and 7) for pure CMC, 75/25 CMC/PVP, pure PVP, and

Table III Mean Values and Standard Deviations of Apex Angles and Widths Measured from the Fabricated Dissolvable (CMC) Microneedles

Design	$\alpha_{mastermold}$ (deg.)	μ_α (deg.)	σ_α (deg.)	$w_{mastermold}$ (μm)	μ_w (μm)	σ_w (μm)	Shrinkage in width (%)
1	45.52	43.89	0.76	502.23	439.51	4.41	12.49
2	31.33	28.84	0.49	313.58	283.67	2.08	9.54
3	30.41	24.27	1.65	169.58	136.10	1.27	19.74
4	32.16	26.83	0.27	210.88	162.35	2.89	23.01
5	31.10	30.12	1.11	151.30	126.66	1.32	16.29
6	32.73	29.82	0.92	252.49	205.67	5.10	18.54
7	45.74	43.60	1.28	262.32	208.88	4.27	20.37

Design numbers refer to those described in Table I

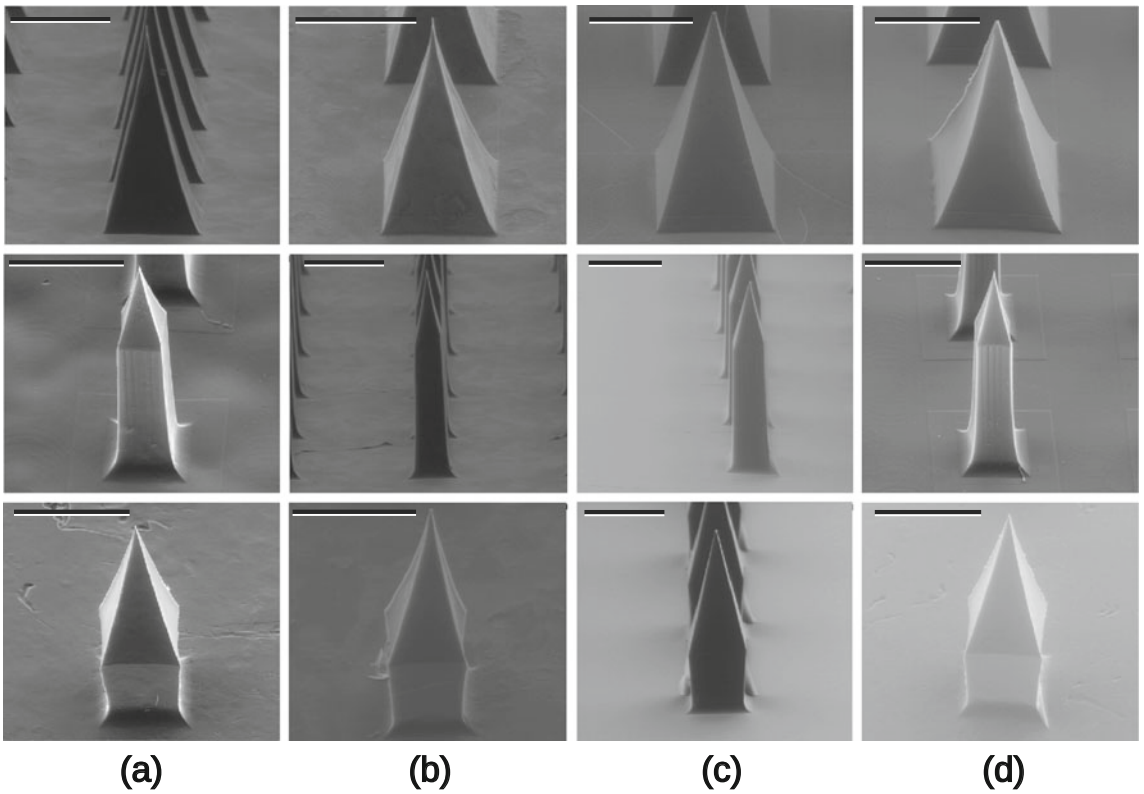

Fig. 12 MNAs (1st row – pyramid microneedles with 30° apex angle, 2nd row – straight obelisk microneedles with 30° apex angle, 200 μm width, and 850 μm height, 3rd row – beveled obelisk microneedles with 30° apex angle) fabricated from different dissolvable materials: (**a**) pure CMC, (**b**) CMC/PVP at 75/25 dry-weight ratio, (**c**) pure PVP, and (**d**) CMC/maltodextrin at 50/50 dry-weight ratio (scale bars correspond to 300 μm). The visible differences arise from different scaling of each figure.

CMC/maltodextrin needles. It is seen that the MNAs are fabricated successfully in each case for different materials and geometries.

In addition to different materials, different array configurations can be fabricated using the presented approach. To demonstrate this, Fig. 13 shows a set of MNAs fabricated considering different array configurations ranging from 6×6 to 10×10 needles.

MNA Directed Delivery to Human and Mouse Skin

Qualitative and Quantitative Assessment of MNA Insertion Into Human Skin

To evaluate cargo delivery, we directly evaluated the deposition of dyes and particulates delivered to human skin using pyramidal and obelisk MNAs. Initially, MNAs were fabricated with

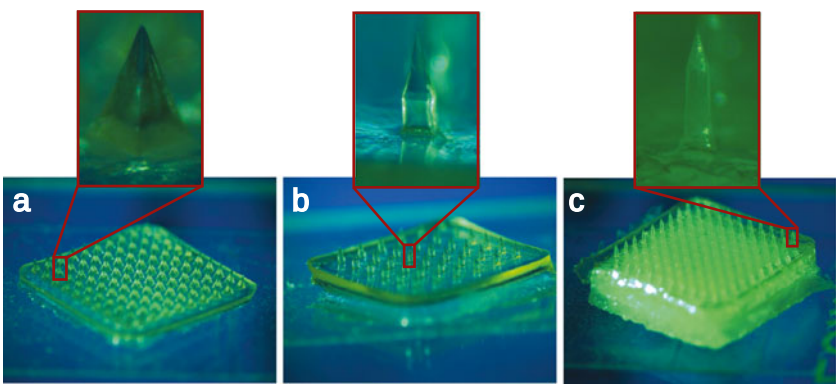

Fig. 13 Optical microscope images of different array configurations: (**a**) a pyramid MNA with 30° apex angle in a 10×10 array, (**b**) a beveled obelisk MNA with 30° apex angle in a 6×6 array, and (**c**) a straight obelisk MNA with 30° apex angle, 200 μm width, and 850 μm height in a 10×10 array.

India ink tracer using 20 wt% CMC hydrogel encapsulating 1% tracer ink as described above. A spring loaded applicator was used to apply the MNAs to living human skin explants. After 15 min, MNAs were removed and the skin surface was photographed using a Zeiss preparative stereo microscope equipped with a CCD camera at 5× optical magnification.

The appearance of the microneedles before and after application of the MNAs to human skin was assessed by scanning electron microscopy (see Fig. 14a–b for pyramidal; Fig. 14e–f for obelisk MNAs). We found a larger portion of the obelisk-type needles dissolved, as in comparison to pyramidal needles. Importantly, while both pyramidal and obelisk needles penetrated the skin, the obelisk design enabled greater and more consistent deposition of needle material, as evaluated by the distribution of the tracer ink in the skin (Fig. 14g–h *vs.* Fig. 14c–d). This was expected since the obelisk geometry was designed to enable more complete insertion of the needles by minimizing the insertion forces and resistance of the skin.

Quantitative assessment of cargo delivery was consistent with these results. To quantitatively assess the cargo delivery of MNAs with different microneedle geometries, OVA-embedded MNAs with ^{3}H tracer were fabricated. The MNAs were then applied to human skin and removed 30 min after exposure, and the deposited ^{3}H content of the excised human skin was determined by scintillation counting. Cumulative data from repeated testing of multiple arrays from multiple production batches (4 batches fabricated independently with at least 4 arrays per batch) showed that the pyramidal needle-geometry resulted in the delivery of an average of $2.1 \pm 19\%$ μg OVA per MNA. In contrast MNAs with obelisk needles delivered $8.2 \pm 6.8\%$ μg OVA per MNA. In both cases, the observed variability included experimental variability related to the anatomic variation in skin samples that were randomized for both subject age and anatomic site of derivation.

The data demonstrates that the CMC-based microneedle arrays with different needle-geometries can deliver bioactive cargo to living human skin, and that delivery efficiency is dependent on microneedle geometry. MNAs with obelisk-type needle geometry afforded an overall 3.89 fold greater deposition of cargo than those with pyramidal needle geometry. This is expected as the pyramidal geometry results in an increase in insertion forces with increasing insertion depth. On the other hand, insertion forces are approximately constant for the obelisk geometry, enabling deeper and more reproducible insertion with greater proportional dissolution of the obelisk needle matrix (as observed in Fig. 14b–d *vs.* 14f–h).

To evaluate the pharmacokinetics of MNA delivery and the effects of structural compositions on drug release, we evaluated time dependent release of OVA from obelisk MNAs fabricated with CMC alone, or CMC/MD or CMC/PVP combinations. For this purpose, we utilized MNA compositions described above, specifically (1) CMC; (2) CMC/PVP at 75/25 dry-weight ratio; (3) CMC/PVP at 50/50 dry-weight ratio; and (4) CMC/maltodextrin at 50/50 dry-weight ratio. In all cases, MNAs were loaded with Alexa488 labeled OVA, and release was measured by determining 488 fluorescence in target skin at successive time points. Inclusion of maltodextrin did not significantly affect release kinetics or maximum release, however, increasing concentrations of PVP resulted in delayed and less efficient release overall (Fig. 15).

Obelisk Microneedle MNAs Deliver Functionally Active Biologics to the Skin Microenvironment

To anatomically evaluate cargo delivery to the skin microenvironmet, MNAs were fabricated with embedded green

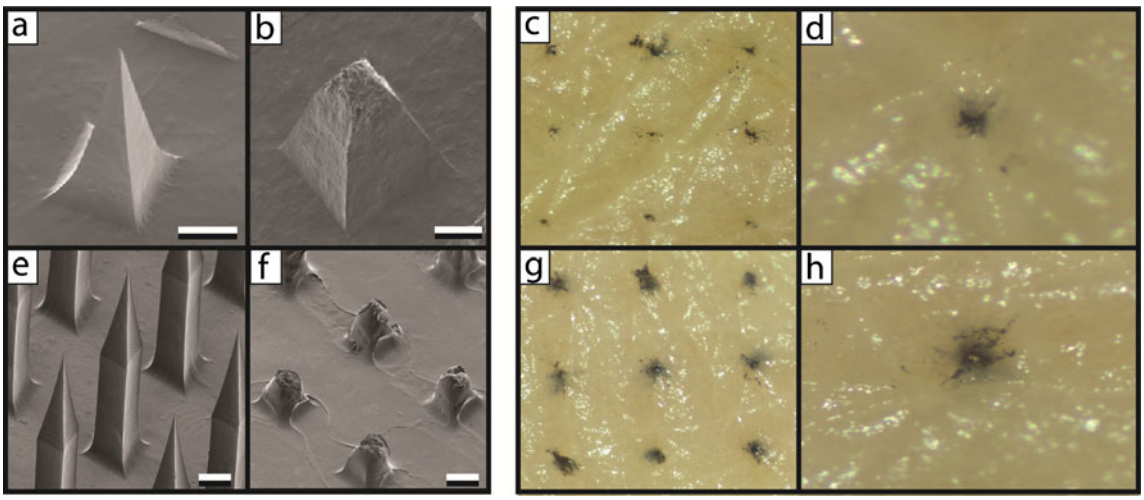

Fig. 14 Microneedle penetration and deposition of cargo. MNAs with pyramidal (**a**–**d**) and obelisk (**e**–**h**) microneedles were trace labeled with India ink and applied to living human skin explants. Needles before (**a**, **e**) and after (**b**, **f**) application, and deposition of cargo in skin (**c**, **d**, **g**, **h**) were evaluated by image analysis (scale bars correspond to 100 μm in **a**, **b**, **d**, **e**, **f**, **h** and 500 μm in **c**, **g**).

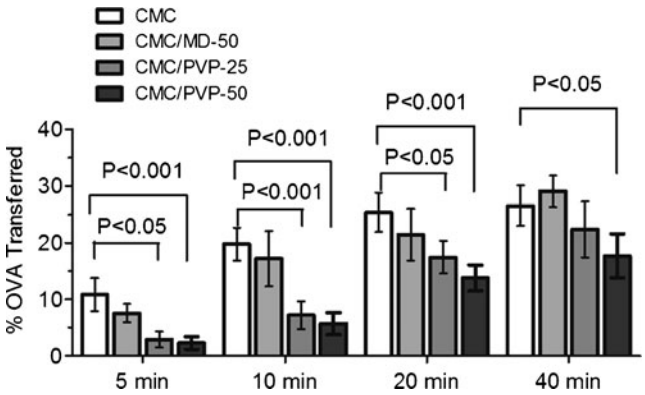

Fig. 15 Kinetics of MNA delivery and the effects of structural composition on cargo release. MNAs incorporating Alexa488-OVA were fabricated with different structural matrices as indicated including CMC (CMC only), CMC/PVP-25 (75% CMC and 25% PVP), CMC/PVP-50 (50% CMC and 50% PVP), and CMC/MD-50 (50% CMC and 50% maltodextrin). MNAs were applied to living human skin for the indicated time intervals and then removed. Targeted skin was excised and assayed for Alexa488 content by spectrofluorometry. Significance and *P*-values were from 4 replicates for each condition using two-way ANOVA.

fluorescent beads (Fluoresbrite YG 1 μm, Polysciences Inc., cat#. 15702). For this purpose, we focused on MNAs with obelisk-type microneedles, since they have considerably better cargo delivery characteristics then those with pyramidal microneedle geometries. The fabricated MNAs with integrated particles were applied to living human skin explants and to the skin of living mice. After 10 min, MNAs were removed, and both targeted human skin and surgically excised skin from sacrificed mice were processed for image analysis. Histopathology of human skin demonstrated periodic visible channels at the sites of individual microneedle penetration (Fig. 16a). Analysis by fluorescence microscopy demonstrated fluorescent bead deposition localized to areas within and surrounding the needle tracks (Fig. 16b). Similarly, analysis of mouse skin macrographs *en face* (obtained from an inverted microscope with a CCD camera) revealed periodic circular green fluorescent bead signal indicative of particle deposition at the sites of microneedle punctures (Fig. 16c). As observed with human skin, serial sections confirmed particle deposition localized in mouse skin at the site of penetration of individual microneedles (Fig. 16c–d), arrows indicate cargo deposition at the sites of three neighboring microneedles.

A potential advantage of MNA technology is the unique opportunity it affords for the specific and precise delivery of embedded cargo to defined microenvironments within the skin. For example, we and others have shown that the skin is rich in dendritic cells and other antigen presenting cells (APCs) essential for vaccine induced immune induction (42). Targeting skin APCs can be an effective strategy for vaccination in general, and in particular for the induction of cell mediated immune responses, including cytotoxic T-cell (CTL) responses essential to prevent or treat many infectious diseases and cancer (41–45). To evaluate delivery of cargo to APC rich skin microenvironments, APCs were identified in serial sections of skin treated with fluorescent particle containing MNAs (as described above). Both in human (Fig. 17a) and mouse (Fig. 17b) skin, we found fluorescent beads anatomically co-localized to microenvironments in the skin that are rich in APCs.

To specifically evaluate immunogenicity, we compared MNA immunization to vaccination by the clinically common intramuscular (IM) needle injection route. In humans and animal models, IM vaccinations can induce effective antibody responses, but are generally ineffective in inducing CTL responses. For MNA immunization, MNAs were fabricated with 50 μg OVA per MNA. To evaluate the integrity of MNA integrated OVA, we analyzed and compared OVA from dissolved MNAs, OVA in stock hydrogel before MNA fabrication, and control OVA in solution by PAGE and OVA-specific ELISA (Fig. 18). Neither detectable degradation nor irreversible aggregation of the OVA was detected in either the CMC-hydrogel or in OVA recovered from MNAs (Fig. 18a). OVA from both preparations demonstrated similar profiles to that of control OVA stock solution. Similarly, OVA-specific antibodies recognized MNA recovered OVA comparably to that of control untreated OVA, suggesting that even conformationally dependent antibody recognition sites were retained intact (Fig. 18b). For immunization, MNAs were applied topically to mouse skin and OVA-specific CTL responses were compared to those elicited by IM needle injection (50 μg) using the standard *in vivo* lytic assay (41–45). As expected, equivalent numbers of antigen-

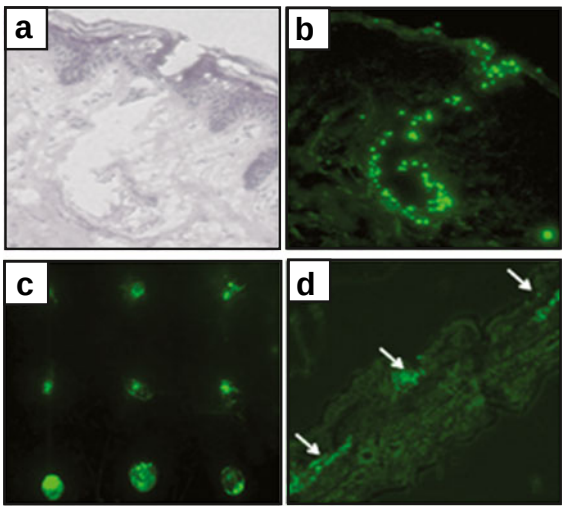

Fig. 16 MNA penetration and cargo delivery to human and mouse skin. MNAs were used to deliver integrated fluorescent particles to living human skin (**a**, **b**) or mice (**c**, **d**). Toluidine blue stained (**a**) and fluorescent microscopic (**b**) images of human skin insertion sites demonstrate delivery cavities penetrating the epidermis and upper dermis, and delivery of fluorescent particles. In (**c**), deposited fluorescent beads delineate the microneedle pattern in skin excised from MNA treated mice. Fluorescent particle deposits are evident in the epidermis and dermis of the same mice (**d**). (**a**, **b**, **d** 20×; **c**, 4× optical magnification).

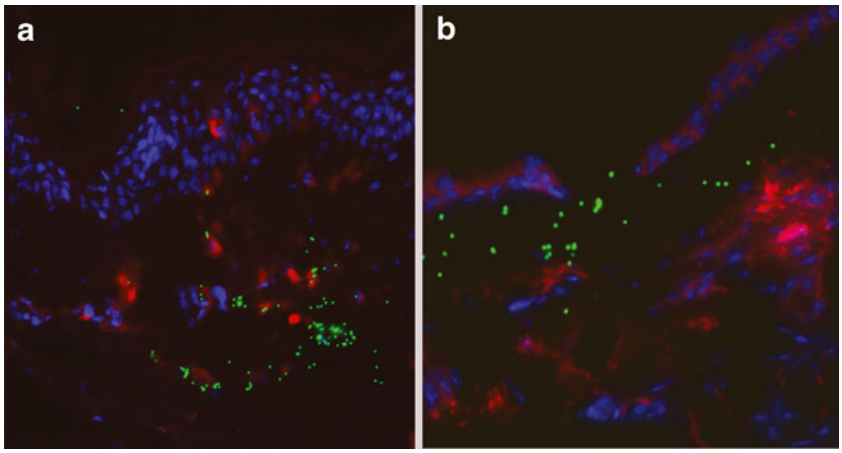

Fig. 17 MNA delivery to antigen presenting cell rich skin microenvironments. MNAs containing florescent particles were applied to either human (**a**) or mouse (**b**) skin. Fluorescent particles (*green*) co-localize to antigen skin microenvironments with antigen presenting (MHC class II + cells, *red*) (*blue*, DAPI-stained cell nuclei).

pulsed (bright) and unpulsed (dim) target cells were recovered from control mice (Fig. 19a). On the other hand, mice immunized with MNA-OVA demonstrated high level OVA-specific lysis *in vivo*, with lower survival and recovery of OVA pulsed targets than unplused targets (Fig. 19b). Minimal differences in recovery of the two populations was observed in IM-OVA immunized mice (Fig. 19c). Quantification of antigen specific lysis by standard techniques confirmed that MNA immunization elicited potent CTL immunity (Fig. 19d). In comparison, IM immunization induced low level responses relative to unimmunized controls.

Taken together, these results demonstrate that these MNAs can efficiently deliver antigens to APC rich microenvironments within the skin to induce potent CTL immune responses, an enabling capability relevant to a broad range of vaccination strategies and skin-targeted therapies

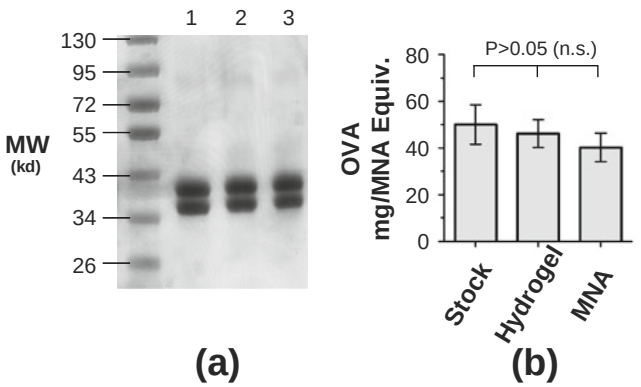

Fig. 18 Integrity of MNA embedded OVA. PAG-electrophoretic analysis (**a**) was used to compare freshly prepared OVA stock solution (Lane 1), OVA recovered from CMC-hydrogel (Lane 2), and OVA recovered from MNAs (Lane 3). For each sample, 5 μg of OVA was electrophoresed on a 12% polyacrylamide gel under reducing conditions. ELISA assays (**b**) were used to compare OVA-specific antibody recognition of serial dilutions of freshly prepared OVA stock solution, OVA recovered from CMC-hydrogel, and OVA recovered from MNAs using biotin-labeled anti-OVA antibody coupled avidin-HRP reporter system. No significant differences ($p > 0.05$) were detected between samples of OVA-stock, OVA in hydrogel and OVA reconstructed from OVA-MNAs.

DISCUSSION

The literature presents strong evidence from *in-vivo* and *in-vitro* studies that dissolvable MNA technology enables delivery of a broad range of bioactive cargo for bolus or sustained delivery. However, developing effective fabrication techniques for dissolvable MNAs will be critical to realize clinically relevant MNA designs that will both meet regulatory requirements and demonstrate improvements in efficacy over existing delivery technologies.

An effective manufacturing technique for dissolvable MNAs should satisfy certain key requirements, including (1) reproducible fabrication capability; (2) applicability to relevant dissolvable materials; (3) capability to create a broad range of microneedle and array geometries; (4) low-temperature processing to prevent harm to bioactive cargo; and (5) low unit cost, short ramp-up time, and scalable (high-throughput) manufacturability. Many of these key requirements are satisfied by the fabrication approaches based on the spin-casting technique. The spin-casting technique has been shown to be applicable to a broad range of materials, capable of low temperature processing, scalability, and low-cost (26,30). The first step in application of the spin-casting technique is to fabricate high-accuracy molds. This can be done by either directly creating the mold (1–3), or by creating a master mold, which can then be replicated to (a large number of) production molds. Each production mold can subsequently be used to create a large number of dissolvable MNAs through spin casting.

In the literature, photolithographic and etching processes have been used to fabricate the master molds for application of the spin-casting technique. Originating from electronics fabrication, the photolithographic processes can create micro-scale geometries accurately and reproducibly. However, they impose strict limitations on the materials that can be processed (e.g., Silicon, silicon-oxides, and a few metals) and the geometries that can be created. Furthermore, they require a considerable amount of ramp-up time from design to fabrication,

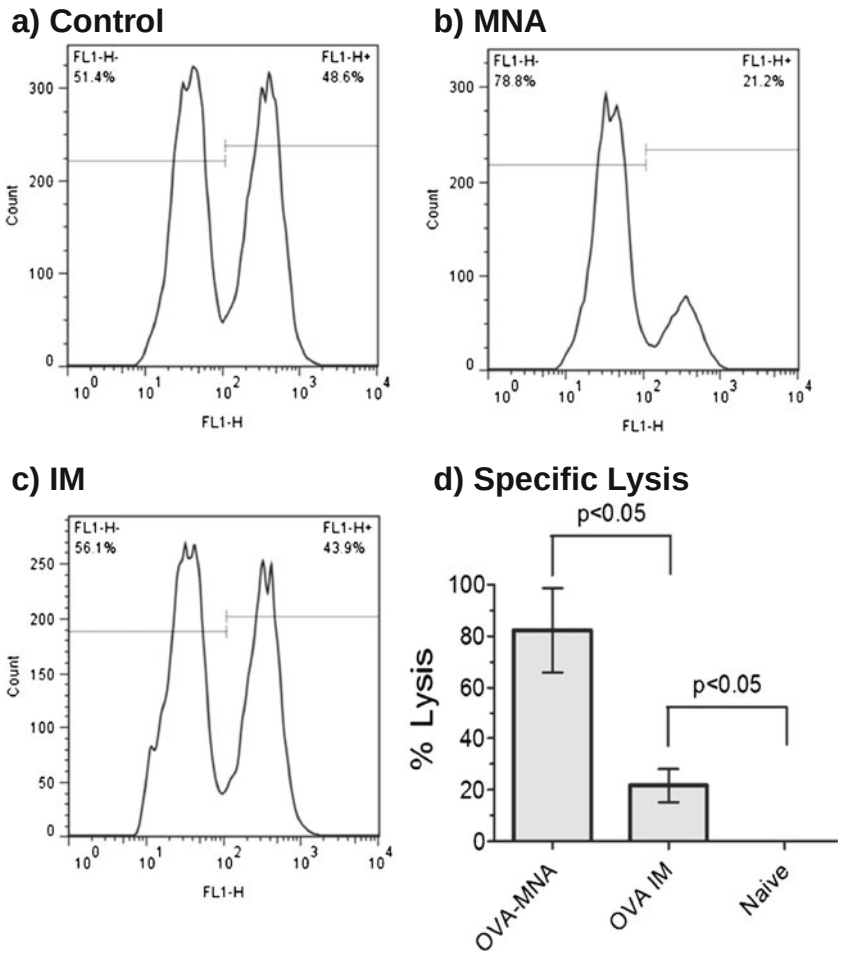

Fig. 19 OVA-MNA directed antigen delivery to the skin microenvironment induces potent CTL immunity. Groups of mice were immunized with OVA-loaded MNAs (OVA MNA) or by IM injection (OVA IM), or were left unimmunized, boosted identically 7 days later. To determine OVA-specific lytic activity, equal numbers of OVA peptide pulsed and unpulsed target cells were injected 5 days later. Prior to injection, target cells were labeled using high (pulsed) or low (unpulsed) concentrations of CFSE. Twenty hours later, animals were sacrificed and target cells recovered and analyzed by flow cytometery with cells with high fluorescence corresponding to retrieved OVA-pulsed targets, and cells with low fluorescence corresponding to unpulsed control target cells. Representative histograms are shown for unimmunized controls (**a**), MNA immunized (**b**), and IM injection immunized (**c**) groups respectively. Quantification of OVA-specific lytic activity is shown in (**d**), based on maximum possible lysis of 100%.

and have high cost, especially for small-to-medium production volumes. Specialized processing conditions (cleanroom processing), use of hazardous chemicals, and expensive production equipment are other requirements of the photolithographic/etching approach. These requirements and shortcomings of photolithography-based master mold fabrication prevent parametric studies and eventual full optimization of microneedle and array designs based on functional requirements.

Here, for the first time, mechanical micromilling as an alternative approach for fabrication of the master molds is presented. During the last decade, many works have demonstrated the utility of the micromilling processes for creating complex geometries on a myriad of materials with high accuracy and repeatability (38,40). A powerful advantage of micromilling technology is its capacity to generate any micro-scale geometry on virtually any type of material in a highly controllable and accurate fashion (38). For micromilling, the lead time for fabricating new designs is measured in minutes-to-hours rather than days or weeks. Metals, most polymers, composites, and even ceramics can be processed through micromilling. Furthermore, the unit cost of parts created by micromilling is very low. Therefore, the use of micromilling could address the disadvantages of photolithographic processes in geometric and material capability, cost, and ramp-up time, while retaining the advantages of accuracy and reproducibility. Furthermore, in contrast to the approach in (30), where a rough milling followed by chemical etching is utilized to fabricate the master molds, no post-processing or hazardous method is used in this work.

We used PMMA as the master mold material: since it is easy to machine, induces negligible tool wear to the micro-scale cutting tools, and provides good wear resistance during elastomer molding, we consider PMMA as an ideal master mold material. Of course, our technique can be applied using alternative mold materials, including metals (e.g., brass, stainless steel, aluminum, titanium) or other polymers.

In common applications of micromilling, micro tools made from tungsten-carbide are used. However, those tools are characterized by relatively blunt (2 μm to 4 μm cutting edge radius) and serrated cutting edges (46). Since the accuracy of microneedles on the master mold is critical, in lieu of the tungsten-carbide micro tools, a set of custom-made single-crystal diamond tools was designed and fabricated for this work: Although significantly more expensive as compared to carbide micro-tools, the diamond micro tools are very sharp (< 300 nm

cutting edge radius), smooth, dimensionally accurate, and significantly more wear resistant. As such, they enable reproducible fabrication of accurate, smooth and defect-free needle geometries with sharp edges and tips.

A prerequisite to fabricating dissolvable MNAs reproducibly is the capability of creating accurate and reproducible master molds. In this paper, we have shown that micromilling can be used to fabricate a broad range of master mold geometries in an accurate and reproducible manner. We quantified the accuracy of the master molds by comparing the dimensions between the targeted and fabricated microneedles on the master molds. To show the range of geometric capability, we considered three different microneedle shapes (pyramid, straight-obelisk, and negative-beveled obelisk) and different dimensional parameters (width, height, and apex angle), totaling seven different needle geometries. We have also analyzed reproducibility by measuring microneedles from different arrays on the same mold, and from different molds.

The reproducibility of the dissolvable MNAs is of utmost importance to their regulatory approval and clinical adaptation. To directly quantify the reproducibility of dissolvable MNAs manufactured through the micromilling/spin-casting approach, we fabricated CMC MNAs for all seven microneedle designs, and measured different geometric dimensions of the microneedles across different arrays: it was shown that dissolvable MNAs from different materials can be fabricated with a very high level of reproducibility. In addition, very sharp needle tips (with tip radii as small as 3 μm) can be fabricated. As expected, a relatively large amount of shrinkage is observed in the dissolvable MNAs due to the drying process. However, it is seen that, for a given geometry, the amount of shrinkage is consistent, resulting in reproducible geometries.

A broad range of matrix materials are available for use in dissolvable microneedles. To demonstrate the application of micromilling/spin-casting fabrication approach to different materials, we produced MNAs from all seven designs using pure CMC, pure PVP, CMC/PVP combinations at different concentrations, and a CMC/maltodextrin (50/50) combination. We observed that, for each case, the targeted designs can be fabricated successfully for different materials, all with room-temperature processing.

We have shown that the dissoluble CMC-based MNAs we fabricated are effective in human and mouse skin penetration. Further, the characteristics of CMC-based dissoluble MNA devices in cargo delivery to bio-targets are strongly geometry dependent. The obelisk-type microneedles delivered four times more cargo for the same array configuration and microneedle height than pyramidal arrays did. Importantly, fluorescent image analysis of the MNA insertion sites in human skin demonstrated that these MNAs were effective in delivering cargo to precise microenvironments within the skin, and in a vaccine application to APC rich microenvironments in the upper dermis and epidermis. Furthermore, data presented here demonstrates that the described fabrication technology enables antigen delivery to the skin microenvironment that results in effective induction of cellular immune responses (CTLs) that are essential for the protection and therapy of many infectious diseases and cancers, and unachievable by clinical "gold-standard" IM injections.

CONCLUSIONS

This paper presents a new technique for fabrication of dissolvable microneedle arrays (MNAs) for intradermal delivery. Although the technique generally follows the elastomer molding and spin-casting approach, for the first time, the master molds are created through mechanical micromilling, thereby enabling fabrication of complex needle and array geometries in an accurate and reproducible fashion. With this capability, parametric studies can be conducted, and optimal yet manufacturable designs can be identified. The fabrication approach uses room-temperature processing, thus enabling retention of the structural integrity and bio-activity of biologics embedded within the MNA material. The capability of the technique is demonstrated by fabricating various needle geometries (pyramid, obelisk, beveled) and array configurations from different dissolvable MNA materials (CMC and PVP, as well as CMC/PVP and CMC/maltodextrin combinations in different ratios). After analyzing the geometric accuracy of micromilled master molds, a statistical analysis of reproducibility of fabricated dissolvable MNAs was conducted through SEM measurement of geometric features (width, apex angle, tip radius). Results demonstrate that the new micromilling/spin-casting based approach is capable of fabricating dissolvable MNAs with complex needle and array geometries reproducibly. The effectiveness of MNAs in piercing the skin, delivering a bioactive cargo to the skin microenvironment, and inducing a cellular immune response is shown in complimentary human and mouse skin studies.

ACKNOWLEDGMENTS AND DISCLOSURES

This study is funded in part by the National Institute of Health Grant R01EB012776. The authors would like to thank Mr. Eric Mellers, a former M.S. student at CMU, for his efforts in the initial stages of the project.

REFERENCES

1. Donnelly RF, Singh TRR, Woolfson AD. Microneedle-based drug delivery systems: microfabrication, drug delivery, and safety. Drug Deliv. 2010;17(4):187–207.
2. Hegde NR, Kaveri SV, Bayry J. Recent advances in the administration of vaccines for infectious diseases: microneedles as painless

delivery devices for mass vaccination. Drug Discov Today. 2011;16:1061–8.
3. Arora A, Prausnitz MR, Mitragotri S. Micro-scale devices for transdermal drug delivery. Int J Pharm. 2008;364(2):227–36.
4. Prausnitz MR, Langer R. Transdermal drug delivery. Nat Biotechnol. 2012;26(11):1261–8.
5. Bouwstra JA. The skin barrier, a well-organized membrane. Colloids Surf. 1997;123:403–13.
6. Kim YC, Park JH, Prausnitz MR. Microneedles for drug and vaccine delivery. Adv Drug Deliv Rev. 2012;64(14):1547–68.
7. Walker RB, Smith EW. The role of percutaneous penetration enhancers. Adv Drug Deliv Rev. 1996;18:295–301.
8. Nair LS, Laurencin CT. Biodegradable polymers as biomaterials. Prog Polym Sci. 2007;32:762–98.
9. Karande P, Mitragotri S. Enhancement of transdermal drug delivery via synergistic action of chemicals. Biochim Biophys Acta. 2009;1788(11):2362–673.
10. Williams AC, Barry BW. Penetration enhancers. Adv Drug Deliv Rev. 2012;64:128–37.
11. Shivanand P, Binal P, Viral D, Shaliesh K, Manish G, Subhash V. Microneedle: various techniques of fabrications and evaluations. Int J ChemTech Res. 2009;1(4):1058–62.
12. Wissink JM, Berenschot JW, Tas NR. Atom sharp microneedles, the missing link in microneedle drug delivery? Proceedings of Medical Devices Conference; 2008.
13. Gill H, Denson D, Burris B. Effect of microneedle design on pain in human subjects. Clin J Pain. 2008;24(7):585–94.
14. Jain RA. The manufacturing techniques of various drug loaded biodegradable poly(lactide-co-glycolide) (PLGA) devices. Biomaterials. 2000;21:2475–90.
15. Khanna P, Luongo K, Strom JA, Bhansali S. Sharpening of hollow silicon microneedles to reduce skin penetration force. J Micromech Microeng. 2010;20(4):045011.
16. Nordquist L, Roxhed N, Griss P, Stemme G. Novel microneedle patches for active insulin delivery are efficient in maintaining glycaemic control: an initial comparison with subcutaneous administration. Pharm Res. 2007;24(7):1381–8.
17. Roxhed N, Gasser T, Griss P. Penetration-enhanced ultrasharp microneedles and prediction on skin interaction for efficient transdermal drug delivery. J Microelectromech Syst. 2007;16(6):1429–40.
18. Matriano JA, Cormier M, Johnson J, Young WA, Buttery M, Nyam K, *et al.* Macroflux microprojection array patch technology: a new and intracutaneous immunization. Pharm Res. 2002;19(1):63–70.
19. Donnelly RF, Singh TRR, Tunney MM, Morrow DIJ, McCarron PA, O'Mahony C, *et al.* Microneedle arrays allow lower microbial penetration than hypodermic needles in vitro. Pharm Res. 2009;26(11):2513–22.
20. Koutsonanos DG, Del Pilar Martin M, Zarnitsyn VG, Sullivan SP, Compans RW, Prausnitz MR, *et al.* Transdermal influenza immunization with vaccine-coated microneedle arrays. PLoS One. 2009;4(3):e4773.
21. Matteucci M, Casella M, Bedoni M, Donetti E, Fanetti M, De Angelis F, *et al.* A compact and disposable transdermal drug delivery system. Microelectron Eng. 2008;85(5–6):1066–73.
22. Wilke N, Hibert C, Brien JO, Morrissey A. Silicon microneedle electrode array with temperature monitoring for electroporation. Sensors Actuators A Phys. 2005;123–124:319–25.
23. Gardeniers HJGE, Luttge R, Berenschot EJW, De Boer MJ, Yeshurun SY, Hefetz M, *et al.* Silicon micromachined hollow microneedles for transdermal liquid transport. J Microelectromech Syst. 2003;12(6):855–62.
24. Park JH, Allen MG, Prausnitz MR. Biodegradable polymer microneedles: fabrication, mechanics and transdermal drug delivery. J Control Release. 2005;104(1):51–66.
25. Park JH, Allen MG, Prausnitz MR. Polymer microneedles for controlled-release drug delivery. Pharm Res. 2006;23(5):1008–19.
26. Park JH, Choi SO, Kamath R, Yoon YK, Allen MG, Prausnitz MR. Polymer particle-based micromolding to fabricate novel microstructures. Biomed Microdevices. 2007;9(2):223–34.
27. Sammoura F, Kang J, Heo YM, Jung T, Lin L. Polymeric microneedle fabrication using a microinjection molding technique. Microsyst Technol. 2006;13:517–22.
28. Lippmann JM, Geiger EJ, Pisano AP. Polymer investment molding: method for fabricating hollow, microscale parts. Sensors Actuators A Phys. 2007;134:2–10.
29. Sullivan SP, Murthy N, Prausnitz MR. Minimally invasive protein delivery with rapidly dissolving polymer microneedles. Adv Mater. 2008;20(5):933–8.
30. Donnelly RF, Majithiya R, Singh TRR, Morrow DIJ, Garland MJ, Demir YK, *et al.* Design, optimization and characterisation of polymeric microneedle arrays prepared by a novel laser-based micromoulding technique. Pharm Res. 2011;28(1):41–57.
31. Lee JW, Park J, Prausnitz MR. Dissolving microneedles for transdermal drug delivery. Biomaterials. 2008;29(13):2113–24.
32. Tsioris K, Raja WK, Pritchard EM, Panilaitis B, Kaplan DL, Omenetto FG. Fabrication of silk microneedles for controlled-release drug delivery. Adv Funct Mater. 2012;22(2):330–5.
33. Donnelly RF, Morrow DIJ, Singh TRR, Migalska K, Mccarron A, Mahony CO, *et al.* Processing difficulties and instability of carbohydrate microneedle arrays. Drug Dev Ind Pharm. 2009;35(10):1242–54.
34. Miyano T, Tobinaga Y, Kanno T, Matsuzaki Y, Takeda H, Wakui M, *et al.* Sugar micro needles as transdermic drug delivery system. Biomed Microdevices. 2005;7(3):185–8.
35. Kolli CS, Banga AK. Characterization of solid maltose microneedles and their use for transdermal delivery. Pharm Res. 2008;25(1):104–13.
36. Moon SJ, Lee SS. A novel fabrication method of a microneedle array using inclined deep x-ray exposure. J Micromech Microeng. 2005;15:903–11.
37. Falo LD Jr, Erdos G, Ozdoganlar OB. Dissolvable microneedle arrays for transdermal delivery to human skin. US Patent No. 0098651; 2011.
38. Filiz S, Xie L, Weiss L, Ozdoganlar OB. Micromilling of microbarbs for medical implants. Int J Mach Tools Manuf. 2008;48(3–4):459–72.
39. Xie L, Brownridge SD, Ozdoganlar OB, Weiss LE. The viability of micromilling for manufacturing mechanical attachment components for medical applications. Transactions of NAMRI/SME 2006;445–52.
40. Wilson ME, Kota N, Kim Y, Wang Y, Stolz DB, LeDuc PR, *et al.* Fabrication of circular microfluidic channels by combining mechanical micromilling and soft lithography. Lab Chip. 2011;11(8):1550–5.
41. Morelli AE, Rubin JP, Erdos G, Tkacheva OA, Mathers AR, Zahorchak AF, *et al.* CD4+ T cell responses elicited by different subsets of human skin migratory dendritic cells. J Immunol. 2005;175(12):7905–15.
42. Larregina AT, Falo LD. Changing paradigms in cutaneous immunology: adapting with dendritic cells. J Investig Dermatol. 2005;124(1):1–12.
43. Condon C, Watkins S, Celluzzi C. DNA–based immunization by in vivo transfection of dendritic cells. Nat Med. 1996;2(10):1122–8.
44. He Y, Zhang J, Donahue C, Falo Jr LD. Skin-derived dendritic cells induce potent CD8(+) T cell immunity in recombinant lentivector-mediated genetic immunization. Immunity. 2006;24(5):643–56.
45. Larregina AT, Watkins SC, Erdos G, Spencer LA, Storkus WJ, Beer Stolz D, *et al.* Direct transfection and activation of human cutaneous dendritic cells. Gene Ther. 2001;8(8):608–17.
46. Aramcharoen A, Mativenga PT, Yang S, Cooke KE, Teer DG. Evaluation and selection of hard coatings for micro milling of hardened tool steel. Int J Mach Tools Manuf. 2008;48(14):1578–84.